Aberrant connective tissue sheath contraction drives premature hair follicle regression by inducing progenitor cell depletion in androgenetic alopecia

Zhili Deng[1, 2, 3, #], Li Yang[1, 2, 3, #], Shixin Duan[1, 2, 3], Mengting Chen[1, 2, 3], Yujin Zhang[4], Fangfen Liu[1, 2, 3], Yan Tang[1, 2, 3], Yunying Wang[1, 2, 3, 5], Jiayun Li[1, 2, 3], San Xu[1, 2, 3], Zheng Wu[1, 2, 3], Ben Wang[1, 2, 3], Zhixiang Zhao[1, 2, 3], Wei Shi[1, 2, 3], Hongfu Xie[1, 2, 3], Guo Li[1, 2, 3, *], Ji Li[1 ,2, 3, 6, *]

[1]Department of Dermatology, Xiangya Hospital, Central South University, Changsha, Hunan, China.

[2]Hunan Key Laboratory of Aging Biology, Xiangya Hospital, Central South University, Changsha, Hunan, China.

[3]National Clinical Research Center for Geriatric Disorders, Xiangya Hospital, Central South University, Changsha, Hunan, China.

[4]Department of Dermatology, The Second Hospital of Hunan University of Chinese Medicine, Changsha, Hunan, China.

[5]Department of Dermatology, Second Affiliated Hospital of Xinjiang Medical University, Urumqi, China.

[6]Lead contact.

[#]These authors contributed equally: Zhili Deng, Li Yang.

[*]Corresponding authors: Ji Li, E-mail: liji_xy@csu.edu.cn; Guo Li, E-mail: liguo237@csu.edu.cn.

Abstract

Androgenetic alopecia (AGA) is characterized by progressive miniaturization of hair, forming a distinctive patterned baldness in the scalp; yet, the mechanisms for hair miniaturization in this disease remain largely unknown. Here by single-cell transcriptome analysis, we describe a concise single-cell atlas, and identify the early changes in cell subpopulations, hair follicle (HF) stem cell fate determination and cell-cell communications in AGA anagen HF units. Thereinto, apoptotic loss of HF progenitor cells is significantly increased, correlated with HF miniaturization in AGA. Mechanistically, enhanced contraction of connective tissue sheath (CTS) activates the mechanosensitive channel PIEZO1, which triggers ectopic apoptosis of progenitor cells in human anagen HFs. Continuous CTS contraction during AGA causes long-term loss of progenitor cells via inducing persistent ectopic apoptosis through PIEZO1, eventually leading to premature hair regression. Most importantly, we show that targeting CTS contraction by ML-7, a selective myosin light chain kinase (MLCK) inhibitor, can obviously improve the growth of HFs from balding scalps of AGA patients. Our study reveals the cellular hierarchies and identifies CTS with increased muscle contraction activity as the key determinant of premature hair regression in AGA, highlighting CTS surrounding human HF as therapeutic targets for treating this disorder.

Introduction

Androgenetic alopecia (AGA), also known as male pattern baldness, is the most common type of baldness, affecting both men and women. Testosterone and androgen receptor (AR) signaling pathway are considered to be necessary for AGA development(Ceruti et al., 2018; Inui and Itami, 2013). Genetic susceptibility loci mapping to AR gene and its neighboring ectodysplasin A2 receptor gene (EDA2R) have also been found in AGA(Liu et al., 2016). Current recognized therapies for AGA include finasteride, minoxidil, platelet-rich plasma (PRP) and low-level laser light therapy (LLLT)(Adil and Godwin, 2017; Katzer

et al., 2019). Among these, finasteride suppresses the activity of 5-a reductase 2 (SRD5A2), which transforms testosterone to dihydrotestosterone (DHT), a more potent AR agonist(Ceruti et al., 2018). Although the potential targets of other therapies remain elusive, additional factors are suggested to be involved in the development of AGA besides AR-related pathways; however, specific instances have not been conclusively identified.

AGA is featured by the progressive and patterned conversion of large terminal hair follicles (HFs) into small vellus HFs (termed as HF miniaturization), which eventually results in balding(Deng et al., 2022). All HFs undergo periodic cycles of growth (anagen), regression (catagen), and rest (telogen) stages throughout the lifetime(Deng et al., 2015). Normally, most human hair follicles will remain in anagen for 2-6 years to produce large terminal hair. But in AGA, the growth phase decreases to only days or weeks, followed by premature entry into hair regression; this leads to an increase in the percentage of resting HFs, generating microscopic hairs in the balding scalp as the HF cycles(Garza et al., 2012; Gu et al., 2022). In HF cycle, the growth of HFs relies on the proliferation and differentiation of HF stem/progenitor cells, whose activities are mainly regulated by the components of HF niche (including dermal papilla (DP), dermal sheath (DS), adipocytes and blood vessels *etc*.)(Deng et al., 2022; Festa et al., 2011; Heitman et al., 2020; Morgan, 2014; Plikus and Chuong, 2014). In balding scalp of AGA, HF stem cells (HFSCs), also known as bulge cells, are basically retained, whereas the number of progenitor cells, a cluster of more actively proliferating cells, is decreased(Garza et al., 2011). This suggests that HFs in AGA balding scalp lack fuels for growth, but the details and underlying mechanism are unclear.

To date, the pathogenetic study of AGA has been scant and limited to histomorphology, global gene analysis and immunohistochemistry due to the fact that most laboratory models are not fully representive of AGA(Lolli et al., 2017; Ntshingila et al., 2021). Single-cell RNA-sequencing (scRNA-seq) has emerged as a powerful tool for dissecting the transcriptome dynamics, cell

heterogeneity, cell lineage tracing and cell-cell communications in complex tissues at uniquely high resolution(Deutsch et al., 2020; Jin et al., 2021; Mereu et al., 2020; Papalexi and Satija, 2018; Potter, 2018). However, to our knowledge, a study regarding scRNA-seq application for exploring the pathogenesis of AGA has never been described.

In this study, we report a comprehensive scRNA-seq analysis on human anagen HF units from 3 conditions: balding frontal and non-balding occipital scalps of patients with AGA, and normal frontal scalps of healthy individuals. With these data, we generated a concise single-cell atlas and elucidated the early cellular and molecular changes in AGA anagen HF units. Importantly, via combining human HF organ culture system, we revealed an unexpected role of connective tissue sheath (CTS), the analogous structure of murine DS in human, in regulating HF progenitor cell survival in the development of AGA. In AGA, CTS contraction is significantly enhanced, resulting in mechanical compression of HF progenitor cells; increased mechanical force activates the mechanosensitive calcium channel PIEZO1, thus induces apoptotic loss of progenitor cells, which eventually leads to premature hair regression. Finally, we demonstrated that targeting CTS contraction by ML-7 can promote the growth of HFs from the balding scalps of AGA patients, even better than minoxidil. These findings illustrate the cellular hierarchies in AGA and emphasize relaxing hair follicle by targeting CTS as a promising therapy for its treatment.

Results

Single-cell RNA-seq reveals cell heterogeneity of androgenetic alopecia and healthy anagen HF units

To dissect the cellular heterogeneity and explore the early changes in AGA development, we obtained anagen HFs from frontal balding (B) scalps and occipital non-balding (NB) scalps of AGA patients, and frontal normal scalps of healthy individuals (HS), to perform scRNA-seq (Fig. 1A). Among these,

anagen HFs of balding scalps were at the early stage of hair miniaturization, isolated from the edge of frontal hairline of AGA patients. First, to identify the hair cycle phase of human HFs, we established an identification system by integrating multiple methods reported previously(Langan et al., 2015; Oh et al., 2016) (Fig. S1). Before conducting scRNA-seq, the HFs were confirmed in anagen phase. After sequencing and stringent cell filtration, 76368 cells were retained for subsequent analyses. Following a standard scRNA-seq data analysis procedure, totally 28 clusters (C0-C27) were retained, which were sufficiently separated from each other (Fig. S2A), and these clusters could be reproduced using cells from each of the 12 samples, suggesting that they are robustly present across different samples and conditions (including HS, NB and B) (Fig. S2B, C).

To dissect the cell types, we first defined the expression pattern of SOX9 (Fig. S2D), a reported marker for hair follicle cells(Zou et al., 2021). By immunohistochemistry, we confirmed that SOX9 is expressed in most cells of hair follicle and almost none in other cells, distinguishing hair follicle cells from other epidermal and dermal cells (Fig. S2E). Based on the expression of SOX9, the above clusters were further identified as 20 different cell types, according to the expression of known lineage markers, including Bulge (KRT15$^+$, CXCL14$^+$), DP (VCAN$^+$, CFD$^+$), DS (ACTA2$^+$, CCN2$^+$), outer root sheat basal (ORS, KRT14$^+$, PTHLH$^+$), ORS suprabasal (ORS SB, KRT17$^+$), inner root sheat (KRT6A$^+$), medulla (KRT85$^+$, KRT31$^+$), proliferating progenitors (PR, MKI67$^+$), endothelial cells (Endo, PECAM1$^+$, VWF$^+$), immune cells (CD3D$^+$), Langerhans (CD207$^+$, CD1A$^+$), Melanocytes (DCT$^+$, MLANA$^+$), Vascular smooth muscle cells/pericytes (vSMC, ACTA2$^+$, RGS5$^+$, RERGL$^+$), Sebaceous gland cells (DCD$^+$, SCD$^+$), sweet gland cells (SwG, KRT8$^+$, KRT18$^+$), interfollicular epidermis spinous (IFE spinous, KRT1$^+$, KRT10$^+$), IFE granular (FLG$^+$, KRT2$^+$); cells highly expressing KRT14 but not SOX9 were defined as IFE basal; Inner II (KRT79$^+$) is the outer layer of Infundibulum and Isthmus which highly expressed KRT14 and KRT6A in the upper HF region; in contrast, Outer II has

149 a relatively low expression of KRT6A(Cui and Schlessinger, 2015; He et al.,
150 2020; Hughes et al., 2020; Joost et al., 2020; Joost et al., 2018; Joost et al.,
151 2016; Liu et al., 2022; Rahmani et al., 2014; Takahashi et al., 2020; Wu et al.,
152 2022; Yang et al., 2017) (Fig. 1B-D; Supplementary Table 1; Fig. S2F-K).

153 To investigate the trajectories among all 20 cell types, monocle3(Cao et al.,
154 2019) was employed to perform the pseudotime analysis with the root node
155 setting at start point of bulge on the SOX9$^+$ HF branch and start point of IFE
156 basal on the SOX9$^-$ IFE branch separately. Our data demonstrate that bulge
157 cells first differentiate into ORS and IRS cells, which then further branch into
158 SOX9$^+$ PR, also known as matrix cells, and finally contribute to medulla (HF)
159 formation. For the SOX9$^-$ IFE branch, IFE basal cells can directly differentiate
160 into SOX9$^-$ PR and IFE spinous cells which finally develop into IFE granular
161 cells (Fig. 1E). These patterns are consistent with the knowledge from previous
162 studies(Wu et al., 2022; Yang et al., 2017).

163 Consistent with the scRNA-seq data, immunostaining analysis showed that
164 KRT15 was highly expressed in bulge HFSCs and moderately expressed in IFE
165 basal cells (Fig.1F), similar to previous observations(Garza et al., 2011; Wu et
166 al., 2022). As an IRS marker, KRT6A was exactly expressed mainly in the IRS
167 and some of the inner layer cells of the infundibulum and isthmus, which are
168 the upward continuation of IRS (Fig.1G and Fig. S2L). Moreover, we verified
169 IFE spinous cells with KRT10 and DS cells with α-SMA (Fig. 1H, I). We
170 determined the relative proportion of each cell type in all samples, showing
171 increased DS and sebaceous gland cells in B anagen HF units compared with
172 NB or HS (Fig. S2M). We next explored the number of differentially expressed
173 genes (DEGs) between B and NB/HS. The results showed that all cell types
174 had differences in various degree (Fig. S2N, Supplementary Table 2),
175 suggesting that anagen HFs undergo significant changes at the early stage of
176 hair miniaturization in AGA.

177 To further explore the potential heterogeneity, bulge cells were subclustered
178 into three distinct subclusters (Fig. 2A), in which the percentage of subcluster

179 1 was reduced in the balding bulge of AGA patients (Fig. 2B). Wilcoxon rank-
180 sum test was used to characterize the marker genes specifically enriched in
181 each subpopulation versus other subpopulations. Top marker genes with
182 avg_log2FC>0.25, pct (minimum fraction in either of the two populations)>0.25
183 and P value<0.05 of each subcluster were showed in Fig. S3A and
184 Supplementary Table 3. Among these, KRT15 was commonly highly expressed
185 (Fig. 2C); CD200 was visibly enriched in subcluster 0 (Fig. 2D), while CD34
186 was mainly enriched in subcluster 1 (Fig. 2E). Consistently, $CD34^+$ bulge cells
187 were indeed decreased in the balding bulge (Fig. 2F). By immunostaining, we
188 defined that $CD200^+$ cells are located in the upper bulge with high stemness
189 (known as HFSCs), while CD34 is mainly expressed in the lower bulge cells
190 referred to as HF progenitor cells, which are differentiated from the upper bulge
191 HFSCs and give rise to matrix cells and produce the new hair shaft (Fig. 2G,
192 H). Via RNA Velocyto analysis, we further confirmed that $CD200^+$ bulge cells
193 are the HFSCs, which have the ability to differentiate into $CD34^+$ progenitor
194 cells (Fig. 2I).

195 PR cells are the proliferating progenitors which highly expressed MKI67.
196 Further subclustering analysis separated PR cells into 2 subclusters (Fig. S3B).
197 Cell composition analysis showed the subcluster 1 decreased in B anagen HFs
198 of AGA (Fig. S3C). Among these two subclusters, one was enriched for
199 epithelial markers (KRT1 and KRT10), representing the IFE proliferating
200 progenitor (ePR) cells; another one (subcluster 1) was specifically enriched for
201 HF cell marker SOX9, suggesting that it represented the HF proliferating
202 progenitors also named as matrix cells (Fig. S3D, E, and Supplementary Table
203 4).

204 Subclustering of DP cells, the signaling center for hair growth(Morgan, 2014),
205 revealed 5 subclusters (Fig. 2J, Fig. S3F and Supplementary Table 5). The
206 percentage and distribution of subclusters were comparable across HS, NB and
207 B, suggesting that DP cell identity may not alter in AGA anagen HFs (Fig. 2K
208 and Supplementary Table 6). Gene ontology (GO) analysis showed that

209 angiogenesis-related pathway was downregulated (Fig. 2L), consistent with our
210 previous findings from bulk RNA sequencing(Deng et al., 2022).

211 DS cells were divided into 4 subclusters (Fig. 2M, Fig. S3G and
212 Supplementary Table 7), which showed no significant changes in the balding
213 anagen HFs of AGA patients (Fig. 2N and Supplementary Table 8). Pathway
214 enrichment analysis of differential genes revealed muscle contraction was
215 obviously upregulated in balding anagen HFs compared to non-balding or
216 healthy groups (Fig. 2O).

217 In human hair follicle, the DS is tightly surrounded by a network of blood
218 vessels, composed of vSMCs and endothelial cells(Martino et al., 2021).
219 Among them, vSMCs were separated into 4 subclusters, and the percentage
220 and distribution of subclusters were comparable across three groups (Fig. 2P,
221 O; Fig. S3H; Supplementary Table 9 and Supplementary Table 10). Pathway
222 enrichment analysis showed that smooth muscle contraction and multiple
223 pathways involved in inflammatory regulation (such as IL-17 signaling pathway)
224 were upregulated in vSMCs of balding anagen HFs (Fig. 2R). Endothelial cells
225 were divided into 4 subclusters, which exhibited no obvious alterations (Fig.
226 S3I-K; Supplementary Table 11 and Supplementary Table 12), and IL-17
227 signaling pathway was also upregulated in endothelial cells of balding anagen
228 HFs (Fig. S3L).

229 Immune cells expressing CD3D were further separated into 6 subclusters,
230 including Th17 cells ($IL17A^+$, $IL17F^+$ and $IL22^+$), naive $CD4^+$ T cells ($IL7R^+$),
231 $CD8^+$ T cells ($GZMK^+$ and $CD8A^+$), natural killer T (NKT) cells ($ZNF683^+$) and
232 two unknown subclusters (Fig. S3M-O; Supplementary Table 13). Cell
233 composition analysis showed significant increase of Th17 cells in balding HF
234 units (Fig. S3P, Q), which provides evidence for inflammatory infiltration in AGA.

235 ***Identification of early changes in HFSC fate determination and cell-cell***
236 ***communications in AGA***

237 Epidermal and sebaceous differentiation of HFSCs has been reported to be
238 associated with HF miniaturization during ageing-induced and obesity-induced

239 hair loss in mice(Matsumura et al., 2016; Morinaga et al., 2021), but it was
240 unclear whether there existed HFSC fate determination alterations in AGA
241 development. To address this question, we conducted cell fate analysis among
242 potential cell types: bulge, ORS, sebaceous gland and IFE basal cells. As
243 expected, more HFSCs showed a pronounced tendency to differentiate into
244 sebaceous gland and IFE basal cells in balding HFs compared with non-balding
245 and healthy HFs, and obviously decreased HFSCs differentiated into ORS cells
246 (Fig. S4A, D). To explore the underlying mechanisms, branched expression
247 analysis modeling (BAEM) was performed, and identified three common cell
248 fate determination genes, COL17A1, PPP1R1C and SGK1 (Fig. S4B, C, E, F).
249 To further characterize the cell-cell communications between different cell
250 types in HF units. Cellchat(Jin et al., 2021) was employed to compare the cell-
251 cell communications between balding and non-balding/healthy HFs. Although
252 the interaction strength showed that most cell types had no obvious changes in
253 incoming and outgoing interaction strength, Th17 cells and langerhans
254 exhibited increased incoming interaction strength in balding and non-balding
255 HFs compared to healthy HFs, while ORS cells displayed decreased outgoing
256 interaction strength in balding anagen HFs in AGA (Fig. S4G).

257 ***Apoptotic loss of HF progenitor cells is correlated with HF miniaturization***
258 ***in AGA***

259 AGA is characterized by the progressive conversion of the terminal (t) scalp
260 HFs into intermediate/miniaturized (i/m) HFs, which we called the process of
261 HF miniaturization and may be attributed to the deficiency of progenitor cells
262 based on our scRNA-seq data as mentioned above and the early study(Garza
263 et al., 2011). To verify changes in HFSC and progenitor cell numbers, we
264 performed immunostaining of CD200 and CD34 on anagen HFs from frontal
265 balding (B) and occipital non-balding scalps (NB) of AGA patients, and frontal
266 normal scalps of healthy individuals (HS). Surprisingly, HFs retain $CD200^{+}$
267 HFSCs with the same percentage in AGA, despite a decrease in cell numbers
268 in B scalps (Fig. S5A-C). In contrast, $CD34^{+}$ progenitor cells were gradually

diminished during the process of HF miniaturization (Fig. 3A-C). Further analysis indicated a strong positive correlation between the number/ proportion of $CD34^+$ progenitor cells and the hair follicle diameter in balding scalps of AGA patients (Fig. 3D-G). Collectively, these observations implicated an intriguing role of progenitor cells in HF miniaturization.

Next, investigation into the causes of the progenitor cell loss via signaling pathway enrichment analysis revealed upregulated apoptotic signals in progenitor cells of balding anagen HFs (Fig. 3H). A significant increase in apoptosis was observed in the $CD34^+$ progenitor cells of balding anagen HFs according to TUNEL staining (Fig. 3I, J). These results support the notion that an apoptosis-induced gradual loss of $CD34^+$ progenitor cells may be involved in the HF miniaturization in AGA.

Hyperactive CTS contraction drives premature hair regression via inducing apoptosis of progenitor cells in AGA

Intimate crosstalk between stem cells and the surrounding microenvironment is vital for stem cell fate decisions. On the outside of the progenitor cells is a layer of elastic DS in murine pelage HF, while in human scalp HF is the multi-layer of connective tissue sheath (CTS) mainly composed of DS cells, collagens and vasculature (including vSMCs and endothelial cells) (Martino et al., 2021)(Fig. S6A; Fig. 4A, B). Pathway enrichment analysis revealed increased contractile activity in both DS cells and vSMCs of balding anagen HFs compared to non-balding or healthy groups (Fig. 2O and R), which can be confirmed by the immunostaining of phosphorylated myosin light chain 2 (p-MLC2), a marker of myosin active state(Nayak et al., 2020) (Fig. 4C, D; Fig. S6B, C). Collectively, these results suggest that CTS contraction is enhanced in anagen HFs of balding scalps in AGA patients.

Given that the contractile force of DS is a key driver of HF regression during hair regeneration in mice(Heitman et al., 2020), we wondered whether excessive contraction of the progenitor cell-encapsulating CTS, the analogous structure of murine DS in human, might affect hair follicle by modulating

299 progenitor cell fate in AGA. To this end, we utilized methacholine (MCH)(Huang
300 et al., 2012; Kudo et al., 2012) and norepinephrine (NE)(Cairns and Borrani,
301 2015; Lynch and Ryall, 2008) to activate CTS contraction in the in vitro cultured
302 human anagen HF organs. The efficiency of MCH and NE on contraction
303 activation in this model was evaluated and verified by p-MLC2 immunostaining
304 (Fig. S6D). Strikingly, HF growth was significantly inhibited (Fig. S6E-G) and
305 premature catagen induction was promoted (Fig. S6H, I) in HFs treated with
306 MCH or NE. Furthermore, the observed activation of CTS contraction by MCH
307 resulted in a dose-dependent negative effect on hair growth and anagen
308 maintenance (Fig. 4E-H, and Fig. S7A, B). To figure out whether progenitor cells
309 act as the targets of CTS contraction, we examined the effect of MCH on the
310 number and apoptosis of HF progenitor cells. The immunostaining of CD34 and
311 TUNEL showed that activated CTS contraction by MCH promoted the loss and
312 apoptosis of $CD34^+$ progenitor cells in a concentration-dependent manner. Of
313 note, $TUNEL^+CD34^+$ cells are barely detectable under 100 μM MCH treatment
314 due to the fact that CD34+ progenitor cells were almost depleted under this
315 condition (Fig. 4I-L).

316 Notably, blockade of CTS contraction with ML-7 (Fig. S7C), a specific myosin
317 activation inhibitor(Colgren and Nichols, 2022), not only improved the growth
318 retardation and catagen premature induction (Fig. 4M-O, and Fig. S7D), but
319 also restored the apoptotic loss of progenitor cells in MCH-treated human HFs
320 (Fig. 4P, Q), confirming the critical role of CTS contraction in MCH effects.
321 Consistently, we demonstrated that the percentage of catagen HFs is indeed
322 markedly increased in the B scalps of AGA patients compared to NB or HS
323 scalps (Fig. 4R-T). Collectively, these findings
324 significantly strengthen the link between enhanced CTS contraction and AGA
325 pathogenesis.

326 Subsequently, to determine whether apoptosis is necessary, we applied Z-
327 VAD-FMK to block cell apoptosis(Li et al., 2019). Our results showed that the
328 observed phenotypes caused by MCH, including HF growth inhibition (Fig. 5A-

329 D), premature catagen induction (Fig. 5E) and depletion of $CD34^+$ progenitor
330 cells (Fig. 5F-H), were counteracted after Z-VAD-FMK administration. Taken
331 together, these data suggest that over-activated CTS contraction compresses
332 hair growth and drives premature hair regression via promoting the apoptosis
333 of progenitor cells.

334 ***CTS contraction induces progenitor cell apoptosis and premature hair***
335 ***regression via PIEZO1 signaling in AGA***

336 To pinpoint the specific molecular mechanisms by which the contractility of CTS
337 regulates progenitor cells, we first examined the expression levels of the known
338 mechanosensitive ion channel protein PIEZO1, which has been found to be
339 highly expressed in HFSCs in mice(Xie et al., 2022). Our results showed that
340 PIEZO1 was abundantly expressed in $CD34^+$ progenitor cells (Fig. S8A) and
341 was expressed at much higher levels in balding anagen HFs compared to non-
342 balding group (Fig. 6A, B). We then used intracellular Ca^{2+} as a downstream
343 indicator of PIEZO1 signaling(Kefauver et al., 2020; Ranade et al., 2015). As
344 quantified by Fluo-4 (a Calcium influx indicator) RFI, there was a significant
345 increase in intracellular Ca^{2+} concentration in $CD34^+$ progenitor cells of balding
346 anagen HFs (Fig. 6C, D). These results suggest that PIEZO1 signaling is
347 activated in progenitor cells of balding anagen HFs.

348 We next investigated whether activation of PIEZO1 is sufficient to induce HF
349 growth retardation and premature regression. To this end, we applied YODA1,
350 a PIEZO1-specific activator to cultured anagen HFs (Fig. S8B, C). Intriguingly,
351 anagen HFs treated with YODA1 displayed a phenotype similar to MCH (Fig.
352 6E-I and Fig. S8D). In addition, the Ca^{2+} concentration in MCH-treated HF
353 progenitor cells was elevated and could be reversed by the specific PIEZO1
354 inhibitor GsMTX4 and the myosin activation inhibitor ML-7 (Fig. 6J, K),
355 indicating the activation of PIEZO1 signaling by CTS contraction. Not
356 surprisingly, inhibition of PIEZO1 signaling by GsMTX4 rescued the phenotypes
357 induced by MCH (Fig. 6L-P).

358 These results prompt us to speculate that CTS contraction induced in balding

359 anagen HFs activates the PIEZO1 signaling pathway in progenitor cells via
360 mechano-transduction, thereby inducing progenitor cell apoptosis and thus
361 promoting premature HF regression.

362 ***Targeting CTS contraction by ML-7 improves the growth of HFs from the***
363 ***balding scalps of AGA patients***

364 All the above results inspired us to wonder whether targeting CTS contraction
365 is a promising therapy for AGA. We first obtained anagen HFs from the balding
366 scalps of AGA patients, which had been experiencing the process of
367 miniaturization. As expected, the balding anagen HFs exhibited obvious growth
368 retardation compared with those from occipital non-balding scalps of the same
369 AGA patients in ex vivo organ culture system (Fig. S9A-C). We then treated the
370 balding HFs with ML-7, or minoxidil (MNX), the FDA-approved drug for AGA
371 treatment. Immunostaining of p-MLC2 confirmed that ML-7 abolished muscle
372 contraction activity in CTS, but MNX did not (Fig. S9D). Excitingly, ML-7 could
373 significantly improve the growth and premature regression of balding HFs of
374 AGA patients, even better than MNX (Fig. 7A-D; Fig. S9E). Consistently, ML-7
375 showed a better effect on decreasing the apoptotic loss of progenitor cells
376 compared with MNX (Fig. 7E, F). Taken together, these findings suggest that
377 relaxing HFs via targeting CTS contraction is a hopeful strategy for AGA therapy.
378

379 **Discussion**

380 Here we have presented what is, to the best of our knowledge, the first and
381 currently the only comprehensive single-cell transcriptome profiling of all
382 cell types within HF units from balding and non-balding scalps of AGA patients
383 compared with healthy individuals. Considering that HFs of balding scalps used
384 in the present study were in anagen phase and at the early stage of hair
385 miniaturization, isolated from the edge of frontal hairline of AGA patients, our
386 high-quality data allowed us to illustrate the early changes in cell
387 subpopulations, the HF cell lineage trajectory and cell-cell communications in
388 AGA in unprecedented detail. Our atlas uncovers at least 16 different broad cell

389 types in human HF unit, which are more than those described in previous
390 scRNA-seq studies(Takahashi et al., 2020; Wu et al., 2022).
391 The reason for this obvious difference could be likely attributed to the
392 optimization of human HF single cell isolation by combining mechanical
393 separation with multienzyme digestion. Based on this, we obtained previously
394 undescribed DP cells and major cell types of CTS (including DS, vSMC and
395 endothelial cells), which are reported to be essential for regulating the growth
396 of hair follicles(Driskell et al., 2011; Heitman et al., 2020; Martino et al., 2021).
397 Delineation of DP and CTS cells at single-cell level provides an opportunity to
398 determine the precise roles of these cells in the pathogenesis of AGA.

399 The hair growth is powered by HFSCs (termed as bulge stem cells) that have
400 the ability to give rise to all epithelial components of the hair follicle(Chen et al.,
401 2020). However, current understanding of the cellular and molecular changes
402 in the bulge in AGA development is limited. Our scRNA-seq data show that
403 bulge stem cells contain two major subclusters: $CD200^{+}$ bulge stem cells and
404 $CD34^{+}$ progenitor cells. Thereinto, the number and percentage of progenitor
405 cells are significantly decreased in the balding anagen HFs of AGA patients.
406 These results are consistent with the previous study showing that balding scalp
407 in men with AGA retains HFSCs but lacks HF progenitor cells(Garza et al.,
408 2011). Besides, we demonstrate that HFSCs are more likely to differentiate into
409 interfollicular epidermal and sebaceous lineages, rather than HF lineage cells,
410 in the balding scalps, which may be responsible for the progressive hair follicle
411 miniaturization and hair thinning in AGA. Similarly, in the case of ageing- and
412 obesity-induced hair loss in mice, those aberrant fate changes also occur in a
413 fraction of HFSCs, which prefer to undergo epidermal and sebocyte
414 differentiation regulated by COL17A1 proteolysis and inflammatory signals
415 respectively, thereby decreasing the HFSC pool and leading to hair follicle
416 miniaturization in a stepwise manner(Matsumura et al., 2016; Morinaga et al.,
417 2021). Here, our data also suggest an important role of COL17A1 in the
418 aberrant differentiation of HFSCs in AGA development. During normal hair

growth, HF stem/progenitor cells proliferate and differentiate to generate hair matrix cells, which rapidly proliferate to produce the hair shaft of growing hair in the end(Martel et al., 2023). Here, we show that the proliferating matrix cells are also decreased in balding HFs in AGA. It is tempting to speculate that the apoptotic loss of progenitor cells contributes to a decrease in matrix cells, which may cause the premature induction of catagen (namely shortening of anagen), and eventually weakens the generation of terminal hair shaft in AGA development.

DP acts as the signaling center to govern the proliferation and differentiation of HF stem/progenitor cells in hair growth(Morgan, 2014; Plikus, 2012). Our previous study demonstrated that androgen receptor (AR) is upregulated in DP cells, which induce apoptosis of microvascular endothelial cells via paracrine signaling in the DP of balding HFs in AGA(Deng et al., 2022). However, in this study, except for the downregulated angiogenesis, our scRNA-seq analysis identifies no other obvious changes in cell subpopulations and signaling pathways, which may be involved in the regulation of hair growth, in DP cells of balding HFs from AGA patients. The reasons for this discrepancy are currently not clear, and further analysis and experimentation will be required to address this point. Although microinflammation has been commonly reported in AGA(Jaworsky et al., 1992; Magro et al., 2011; Martinez-Jacobo et al., 2018; Peyravian et al., 2020), the details remain largely undefined. Here, we identity that T cells are the main lymphocytes in human HF units, and AGA is featured by increased Th17 cells.

Although a previous study has identified that progenitor cells are significantly diminished by flow cytometry in the bald scalp of AGA patients(Garza et al., 2011), the details in this aspect are obscure. In this study, we further confirm that $CD34^+$ progenitor cells are decreased in the balding anagen HFs in AGA, and determine that these progenitor cells are derived from $CD200^+$ bulge stem cells via scRNA-seq analysis and immunostaining. Importantly, we also find that the reduction in HF progenitor cells is attributed to the increased apoptosis, and

449 the number and percentage of these cells is positively correlated with the hair
450 follicle size in the balding scalp in AGA. These findings suggest a pivotal role
451 for progenitor cell depletion in the pathogenesis of AGA.

452 HF growth is tightly spatiotemporally regulated by the crosstalk between
453 stem/progenitor cells and the microenvironment, mainly the mesenchymal
454 niche(Plikus and Chuong, 2014). In addition to DP whose role is well
455 recognized, DS is also an important component of the mesenchymal niche. DS
456 is continuous with the DP and generates an envelope surrounding the
457 hair follicle, whose role has been far less examined than the DP yet may be
458 equivalently important for the regulation of hair growth(Martino et al., 2021).
459 Until recently, DS has been identified as smooth muscle that drives hair follicle
460 regression for reuniting HFSCs and niche to regenerate tissue structure during
461 hair regeneration in mice(Heitman et al., 2020). Further study demonstrates
462 that progenitor cell-derived endothelin governs DS contraction in mice(Martino
463 et al., 2023). However, the role of CTS (the analogous structure of murine DS
464 in human), in human hair follicle, especially in hair disorders, remains undefined.
465 In this study, via single-cell sequencing analysis we identify that smooth muscle
466 contraction activity is markedly increased in the major cell types of CTS,
467 including DS and vSMC cells in balding anagen HFs of AGA patients. We further,
468 by co-immunostaining, confirm this conclusion, and demonstrate that muscle
469 contraction-related pathways are hyperactivated in the CTS of balding anagen
470 HFs; In human hair follicle organ culture system, activation of muscle
471 contraction in CTS drives premature hair follicle regression via inducing
472 progenitor cell apoptosis. Surprisingly, we find that pharmacological inhibition
473 of muscle contraction can obviously improve the growth and premature catagen
474 induction of hair follicles from the balding scalps of AGA patients, even better
475 than the FDA-approved drug minoxidil, strongly suggesting that targeting
476 muscle contraction in CTS is a very promising therapy for AGA. It will also be
477 interesting in future studies to determine the mechanism that hyperactivates the
478 muscle contraction of CTS cells in the development of AGA.

479 Our results suggest PIEZO1, a mechanosensitive ion channel, as a regulator
480 in HF progenitor cells that senses the mechanical force generated by CTS
481 contraction. We show that PIEZO1 is expressed in HF progenitor cells, and it
482 becomes markedly upregulated and activated in the balding anagen HFs of
483 AGA patients. Inhibition of PIEZO1 signaling evidently alleviates progenitor cell
484 apoptosis and premature hair follicle regression induced by CTS contraction; in
485 contrast, PIEZO1 hyperactivation induces apoptosis of progenitor cells and
486 premature entry into regression in human anagen hair follicles. Similarly,
487 PIEZO1 has been reported to be abundantly expressed in HFSCs, and is
488 responsible for niche-size-decrease-triggered ectopic HFSC apoptosis in
489 mice(Xie et al., 2022). We conclude that the role of PIEZO1 in sensing the
490 abnormal mechanical force from the microenvironment to regulate the HFSC
491 apoptosis is conserved across species, and the mechanosensitive channel
492 might be a therapeutic target for hair loss. However, the detailed molecular
493 mechanisms by which aberrant PIEZO1 activation induces progenitor cell
494 apoptosis in AGA need further study to clarify.
495 In summary, the present study reveals the cellular hierarchies via scRNA-seq
496 analysis and demonstrates hyperactive CTS contraction as a critical cause of
497 hair miniaturization in AGA, strongly suggesting that relaxing hair follicle by
498 targeting CTS might be a promising therapy for this disorder.
499

500 **Methods**

501 **Human scalp and HF samples**

502 Human scalp skin biopsies and HF units were collected from non-balding
503 occipital and balding frontal sites of male AGA patients undergoing hair
504 transplantation surgery, and normal frontal sites of male healthy volunteers from
505 the Department of Dermatology in Xiangya Hospital, Central South University.
506 The procedures were in accordance with protocols set out in the WMA
507 Declaration of Helsinki and the Department of Health and Human Services
508 Belmont Report and approved by the ethical committee of the Xiangya Hospital

of Central South University and written informed consent was acquired from all participants.

Identification of hair cycle phases in human HFs

Hair cycle phases of human HFs were determined by morphological analysis, HE staining, co-immunostaining of Ki67 and TUNEL as previously described(Langan et al., 2015; Oh et al., 2016). With these identification methods (Fig. S1), all human HFs used in this study (including scRNA-seq, staining and in vitro organ culture) had been confirmed in the typical anagen phase before experimentation unless otherwise stated.

Preparation of single-cell suspensions of HF units

To obtain single-cell suspension of entire HF units, DPs were isolated first by micro-dissection from HFs and were chopped. The remaining hair follicle tissue samples were cut with scissors and digested with the chopped DPs in 4mg/ml Dispase II and Collagenase IV for 40 min at 37℃, centrifuged at 200g for 5min. The pellet was resuspended and digested in 0.25% trypsin for 10 min at 37℃, washed in PBS+5%FBS and filtered through a 70 μm cell strainer. The Dead Cell Removal Kit (Miltenyi Biotec) was used in accordance with the manufacturer's instruction to obtain live cells. 10 μL of the cell suspension were mixed with the same volume of Trypan blue for cell counting. The loading volume for sequencing was verified by the cell concentration

ScRNA-seq

scRNA-seq mainly includes GEM (gel bead-in-emulsion) generation, barcoding, cDNA amplification, library construction and sequencing. These steps were completed according to the user's instructions of Chromium Single Cell 3' Reagent Kits v3.1 (10× Genomics, product code: 1000268, 1000215, 1000120) (https://www.10xgenomics.com/support/single-cell-gene-expression). Libraries were sequenced by an Illumina NovaSeq6000 System. Approximately 10,000 cells (targeting 5000–12,000) per sample were used for single-cell RNA sequencing.

ScRNA-seq data processing and cell type identification

539 We used the default parameters of Cell Ranger software suite (v6.0.2) to align
540 and quantify the raw reads data from 10x Genomics. After the initial Cell Ranger
541 metric assessment, Seurat (v4.3.0)(Hao et al., 2021) in R version 4.3.1 was
542 used to exclude cells with fewer than 200 genes or more than 6000 genes
543 detected, and more than 20% mitochondrial reads for downstream analysis.

544 After quality control, 76368 cells remained and were used for downstream
545 bioinformatic analysis. The “NormalizeData” function was used to normalize the
546 feature expression measurements for each cell by the total expression. The
547 “ScaleData” function was used to scale and center the expression of each gene
548 for dimensional reduction. To avoid batch effects among samples and
549 experiments, we integrated data from all samples using harmony (v0.1.1). Total
550 cell clustering was performed by “FindClusters”function with Louvain algorithm
551 at a resolution of 0.2. Non-linear dimensional reduction was performed by
552 “RunUMAP” function and visualized by Uniform Manifold Approximation and
553 Projection (UMAP). Markers genes of each cell cluster were determined by
554 “FindAllMarkers” function with Wilcoxon rank-sum test. Only those with
555 |‘avg_logFC’| ≥0.25 and ‘adjusted P value’≤0.05 were considered as marker
556 genes.

557 For subgroup cell clustering, cells of each cell type were extracted separately
558 and clustered by their first 20 PCs and appropriate resolution. To further
559 approximate the low-dimensional data manifold representing the differentiation
560 trajectory for Bulge cells, spliced status of mRNAs in single-cell RNA
561 sequencing data were used to estimations of RNA velocities through
562 velocyto(La Manno et al., 2018). Markers genes of each subcluster were
563 identified by “FindAllMarkers” function with the default parameters.
564 “DoHeatmap” function were used to show top marker genes in heatmap.

565 **Identification of balding-associated DEGs**

566 We used the function of “FindMakers” in Seurat to identify balding-vs-
567 nonbalding and balding-vs-healthy differentially expressed genes (DEGs) for
568 each cell type and sub-cell type. The adjusted P values of each DEG were

569 calculated by non-parametric two-sided Wilcoxon rank-sum test and only those
570 with |'avg_logFC'| > 0.25 and 'adjusted P value' < 0.05 were considered to be
571 balding-associated DEGs.

572 **Function enrichment analysis**

573 Gene Set Enrichment Analysis (GSEA) of GO and KEGG was performed by
574 clusterProfiler R package (v4.5.1.902) and visualized with ggplot2 R package
575 (v3.4.1)(Bechhofer et al., 1986). Representative terms selected from the top
576 ranked GO terms and KEGG pathways from MsigDB were displayed.

577 **Pseudotime analysis**

578 Monocle3 was used to reconstruct the differentiation trajectory for all cell
579 types(Cao et al., 2019). The expression matrix of all cells was used as input
580 and the UMAP embedding coordinates were import from Seurat result. The
581 start points of bulge and IFE basal cells were specified as the root nodes
582 separately for the $SOX9^+$ HF branch and $SOX9^-$ IFE branch of the trajectory
583 graph by "order_cells" function. "Plot_cells" function was used to visualize each
584 cell type along the pseudotime trajectory. To further reconstruct the
585 differentiation trajectory and do "branched expression analysis modeling"
586 (BAEM) for bulge cell fate cell determination related cell types, such as bulge
587 to ORS and IFE, Monocle2(Qiu et al., 2017) was used to reconstruct the
588 differentiation trajectory for small set of cell types and "BAEM" function were
589 performed to identify cell determination related molecules.

590 **Cell-cell communication analysis**

591 To assess cell-cell communications among different cell types, we used cellchat
592 (v1.1.3) to infer the intercellular communication network from single-cell RNA-
593 seq data. Only cell types with more than 10 cells were considered in the
594 analysis. The "trimean" method is used for calculating the average gene
595 expression per cell group in "computeCommunProb" function. Pairwise
596 comparison and visualization are performed by cellchat build-in function, only
597 interactions with P value lower than 0.05 are considered to be real.

598 **HF organ culture**

599 Human HFs were obtained from the non-balding occipital sites
600 (unless stated otherwise) of male AGA patients undergoing hair transplantation
601 surgery. After microdissection, the HFs were first incubated in William'E
602 medium (WEM, ThermoFisher) for 24 hours to re-equilibrate. HFs in anagen VI
603 phase were randomly assigned to the different experimental groups. HFs were
604 cultured at 37℃ with 5% CO_2 in WEM supplemented with 2 mM of L-glutamine,
605 10 ng/ml hydrocortisone, 10 ug/ml insulin and 1% penicillin/streptomycin mixure,
606 and photographed under a stereoscope every two days to count hair shaft
607 length and hair cycle stage. The hair cycle stage (anagen/early-catagen/mid-
608 catagen) of HFs was determined according to the identification methods
609 described above(Langan et al., 2015; Oh et al., 2016).

610 **Chemical stimulation of HFs**

611 All the chemicals were purchased from Selleck. After 24 hours, medium was
612 replaced and HFs were treated with vehicle (0.1% DMSO), MCH (0.1,1 10,100
613 μM as indicated), NE (0.1 μM), ML-7(0.3 μM), Z-VAD-FMK (10 μM), YODA1(15
614 μM), or GsMTX4(1 μM) according to the design of different experiments and
615 the medium was changed daily with the indicated treatment. HFs were cultured
616 for 2-10 days for analysis of hair growth and immunostaining.

617 **Immunostaining and TUNEL staining**

618 Immunostaining was performed as previously described(Deng et al., 2021).
619 Briefly, OCT-embedded samples were sectioned (10 μm) with a Leica cryostat.
620 The sections were fixed for 10 min with 4% PFA, and washed with PBS, then
621 blocked for 60 min with blocking buffer (5% NDS, 1% BSA, 0.3% Triton X-100).
622 Primary antibodies were incubated overnight at 4℃. Secondary antibody was
623 incubated for 60 min at room temperature. After washed, sections were
624 counterstained with DAPI. TUENL staining was performed with TUNEL assay
625 kit (Roche, USA) according to manufacturer's instructions, and then stained
626 with CD34 following the immunostaining protocol. For the co-immunostaining
627 of two antibodies from the same host species, double immunohistochemistry
628 for paraffin sections (8 μm) was conducted by using the Opal 4 color manual

629 immunohistochemistry (IHC) kit (NEL810001KT, PerkinElmer). The signal of p-
630 MLC2 was amplified by the Opal 4 color manual IHC kit (NEL810001KT,
631 PerkinElmer). All pictures were taken with a Zeiss Axioplan 2 microscope. The
632 fluorescence intensity was evaluated with ImageJ. The primary antibodies were
633 used in this study: Rabbit anti-SOX9 (1:100, Cell Signaling), Mouse anti-K15
634 (1:2000, Lab vision), Mouse anti-K14 (1:4000, Abcam), Rabbit anti-KRT6A
635 (1:500, Atlas Antibodies), Rabbit anti-KRT10 (1:1000, Abcam), Mouse anti-α-
636 SMA (1:4000, Abcam), Rabbit anti-CD200 (1:200, Cell Signaling), Rabbit anti-
637 CD34 (1:250, Abcam), Rabbit anti-p-MLC2 (1:100, Cell Signaling), Rabbit anti-
638 Ki67 (1:500, Abcam), Rabbit anti-PIEZO1 (1:100, Proteintech). Staining
639 intensity was evaluated in well-defined reference by quantitative (immuno-)
640 histomorphometry using NIH ImageJ software.

641 **In vitro Ca^{2+} imaging**

642 HFs were incubated with Fluo-4 staining solution (Beyotime) in culture medium
643 at 37℃ for 1 hour. Afterward HFs were washed with DPBS and cultured DPBS
644 with 1mM calcium. For different treatments, MCH, ML-7, YODA1 or GsMTX4
645 was added to the culture medium for 30 min. The HFs were embedded in OCT
646 and were sectioned with a Leica cryostat. Images were taken immediately to
647 record the fluorescence intensity to indicate Ca^{2+} concentration and the
648 adjacent section was used for CD34 staining to indicate progenitor cells.

649 **Statistical analysis**

650 All data were expressed as mean±SEM and were analyzed by ANOVA or
651 Kruskall-Wallis test when more than two groups were compared or Student's t-
652 test when only two groups were compared. Graphpad Prism 8, R (v4.1.3) and
653 Excel (Microsoft) were used to assess statistical significance. Statistical
654 significance was set at a $P < 0.05$. *, ** and *** indicate $P < 0.05$, $P < 0.01$ and
655 $P < 0.001$, respectively.

656 **Data availability**

657 All data needed to assess the conclusions in the present study are provided in
658 the manuscript and/or the Supplementary Materials. The scRNA-seq datasets

are available from the genome sequence archive under accession number HRA005629 (http://bigd.big.ac.cn/gsa-human/). Any other data supporting the findings of this study are available from the corresponding author upon reasonable request.

Acknowledgements

This work was supported by the National Key Research and Development Program of China (No. 2021YFF1201205), the National Natural Science Funds for Distinguished Young Scholars (No. 82225039), the National Natural Science Foundation of China (No. 82304057, No. 81874251, No. 82073457, No. 82173448, No. 82373508, No. 82303992), the Natural Science Funds of Hunan province for excellent Young Scholars (No. 2023JJ20094). We thank our colleagues (Department of Dermatology, Xiangya Hospital, Central South University, China) for their generous support throughout this work.

Author contributions

J.L., Z.D., G.L. and L.Y. designed and conceived the study. Z.D., G.L. and L.Y. performed data analyses. L.Y. and Z.D. performed scRNA-seq analysis. G.L., Z.D., S.D. and M.C. performed most experiments. Y.Z., F.L., Y.T., Y.W., S.X., Z.W., B.W., Z.Z. and W.S. contributed to sample collection. Z.D. and M.C. help to generate sequencing libraries. H.X. and Y.Z. provide critical discussion and suggestion. Z.D., G.L., L.Y. and J.L. prepared the manuscript with input from coauthors.

Competing interests

The authors declare no competing interests.

References

Adil, A., and Godwin, M. (2017). The effectiveness of treatments for androgenetic alopecia: A systematic review and meta-analysis. J Am Acad Dermatol *77*, 136-141 e135.

689 Bechhofer, D.H., Kornacki, J.A., Firshein, W., and Figurski, D.H. (1986). Gene control in broad host range
690 plasmid RK2: expression, polypeptide product, and multiple regulatory functions of korB. Proc Natl Acad
691 Sci U S A *83*, 394-398.
692 Cairns, S.P., and Borrani, F. (2015). beta-Adrenergic modulation of skeletal muscle contraction: key role
693 of excitation-contraction coupling. J Physiol *593*, 4713-4727.
694 Cao, J., Spielmann, M., Qiu, X., Huang, X., Ibrahim, D.M., Hill, A.J., Zhang, F., Mundlos, S., Christiansen,
695 L., Steemers, F.J.*, et al.* (2019). The single-cell transcriptional landscape of mammalian organogenesis.
696 Nature *566*, 496-502.
697 Ceruti, J.M., Leiros, G.J., and Balana, M.E. (2018). Androgens and androgen receptor action in skin and
698 hair follicles. Mol Cell Endocrinol *465*, 122-133.
699 Chen, C.L., Huang, W.Y., Wang, E.H.C., Tai, K.Y., and Lin, S.J. (2020). Functional complexity of hair follicle
700 stem cell niche and therapeutic targeting of niche dysfunction for hair regeneration. J Biomed Sci *27*,
701 43.
702 Colgren, J., and Nichols, S.A. (2022). MRTF specifies a muscle-like contractile module in Porifera. Nat
703 Commun *13*, 4134.
704 Cui, C.Y., and Schlessinger, D. (2015). Eccrine sweat gland development and sweat secretion. Exp
705 Dermatol *24*, 644-650.
706 Deng, Z., Chen, M., Liu, F., Wang, Y., Xu, S., Sha, K., Peng, Q., Wu, Z., Xiao, W., Liu, T.*, et al.* (2022).
707 Androgen Receptor-Mediated Paracrine Signaling Induces Regression of Blood Vessels in the Dermal
708 Papilla in Androgenetic Alopecia. J Invest Dermatol *142*, 2088-2099 e2089.
709 Deng, Z., Chen, M., Liu, Y., Xu, S., Ouyang, Y., Shi, W., Jian, D., Wang, B., Liu, F., Li, J.*, et al.* (2021). A
710 positive feedback loop between mTORC1 and cathelicidin promotes skin inflammation in rosacea.
711 EMBO Mol Med *13*, e13560.
712 Deng, Z., Lei, X., Zhang, X., Zhang, H., Liu, S., Chen, Q., Hu, H., Wang, X., Ning, L., Cao, Y.*, et al.* (2015).
713 mTOR signaling promotes stem cell activation via counterbalancing BMP-mediated suppression during
714 hair regeneration. J Mol Cell Biol *7*, 62-72.
715 Deutsch, A., McLellan, B.N., and Shinoda, K. (2020). Single-cell transcriptomics in dermatology. JAAD Int
716 *1*, 182-188.
717 Driskell, R.R., Clavel, C., Rendl, M., and Watt, F.M. (2011). Hair follicle dermal papilla cells at a glance. J
718 Cell Sci *124*, 1179-1182.
719 Festa, E., Fretz, J., Berry, R., Schmidt, B., Rodeheffer, M., Horowitz, M., and Horsley, V. (2011). Adipocyte
720 lineage cells contribute to the skin stem cell niche to drive hair cycling. Cell *146*, 761-771.
721 Garza, L.A., Liu, Y., Yang, Z., Alagesan, B., Lawson, J.A., Norberg, S.M., Loy, D.E., Zhao, T., Blatt, H.B.,
722 Stanton, D.C.*, et al.* (2012). Prostaglandin D2 inhibits hair growth and is elevated in bald scalp of men
723 with androgenetic alopecia. Sci Transl Med *4*, 126ra134.
724 Garza, L.A., Yang, C.C., Zhao, T., Blatt, H.B., Lee, M., He, H., Stanton, D.C., Carrasco, L., Spiegel, J.H., Tobias,
725 J.W.*, et al.* (2011). Bald scalp in men with androgenetic alopecia retains hair follicle stem cells but lacks
726 CD200-rich and CD34-positive hair follicle progenitor cells. J Clin Invest *121*, 613-622.
727 Gu, Y., Bian, Q., Zhou, Y., Huang, Q., and Gao, J. (2022). Hair follicle-targeting drug delivery strategies for
728 the management of hair follicle-associated disorders. Asian J Pharm Sci *17*, 333-352.
729 Hao, Y., Hao, S., Andersen-Nissen, E., Mauck, W.M., 3rd, Zheng, S., Butler, A., Lee, M.J., Wilk, A.J., Darby,
730 C., Zager, M.*, et al.* (2021). Integrated analysis of multimodal single-cell data. Cell *184*, 3573-3587 e3529.
731 He, H., Suryawanshi, H., Morozov, P., Gay-Mimbrera, J., Del Duca, E., Kim, H.J., Kameyama, N., Estrada,
732 Y., Der, E., Krueger, J.G.*, et al.* (2020). Single-cell transcriptome analysis of human skin identifies novel

733 fibroblast subpopulation and enrichment of immune subsets in atopic dermatitis. J Allergy Clin Immunol
734 *145*, 1615-1628.
735 Heitman, N., Sennett, R., Mok, K.W., Saxena, N., Srivastava, D., Martino, P., Grisanti, L., Wang, Z., Ma'ayan,
736 A., Rompolas, P.*, et al.* (2020). Dermal sheath contraction powers stem cell niche relocation during hair
737 cycle regression. Science *367*, 161-166.
738 Huang, F., Zhang, H., Wu, M., Yang, H., Kudo, M., Peters, C.J., Woodruff, P.G., Solberg, O.D., Donne, M.L.,
739 Huang, X.*, et al.* (2012). Calcium-activated chloride channel TMEM16A modulates mucin secretion and
740 airway smooth muscle contraction. Proc Natl Acad Sci U S A *109*, 16354-16359.
741 Hughes, T.K., Wadsworth, M.H., 2nd, Gierahn, T.M., Do, T., Weiss, D., Andrade, P.R., Ma, F., de Andrade
742 Silva, B.J., Shao, S., Tsoi, L.C.*, et al.* (2020). Second-Strand Synthesis-Based Massively Parallel scRNA-Seq
743 Reveals Cellular States and Molecular Features of Human Inflammatory Skin Pathologies. Immunity *53*,
744 878-894 e877.
745 Inui, S., and Itami, S. (2013). Androgen actions on the human hair follicle: perspectives. Exp Dermatol
746 *22*, 168-171.
747 Jaworsky, C., Kligman, A.M., and Murphy, G.F. (1992). Characterization of inflammatory infiltrates in
748 male pattern alopecia: implications for pathogenesis. Br J Dermatol *127*, 239-246.
749 Jin, S., Guerrero-Juarez, C.F., Zhang, L., Chang, I., Ramos, R., Kuan, C.H., Myung, P., Plikus, M.V., and Nie,
750 Q. (2021). Inference and analysis of cell-cell communication using CellChat. Nat Commun *12*, 1088.
751 Joost, S., Annusver, K., Jacob, T., Sun, X., Dalessandri, T., Sivan, U., Sequeira, I., Sandberg, R., and Kasper,
752 M. (2020). The Molecular Anatomy of Mouse Skin during Hair Growth and Rest. Cell Stem Cell *26*, 441-
753 457 e447.
754 Joost, S., Jacob, T., Sun, X., Annusver, K., La Manno, G., Sur, I., and Kasper, M. (2018). Single-Cell
755 Transcriptomics of Traced Epidermal and Hair Follicle Stem Cells Reveals Rapid Adaptations during
756 Wound Healing. Cell Rep *25*, 585-597 e587.
757 Joost, S., Zeisel, A., Jacob, T., Sun, X., La Manno, G., Lonnerberg, P., Linnarsson, S., and Kasper, M. (2016).
758 Single-Cell Transcriptomics Reveals that Differentiation and Spatial Signatures Shape Epidermal and Hair
759 Follicle Heterogeneity. Cell Syst *3*, 221-237 e229.
760 Katzer, T., Leite Junior, A., Beck, R., and da Silva, C. (2019). Physiopathology and current treatments of
761 androgenetic alopecia: Going beyond androgens and anti-androgens. Dermatol Ther *32*, e13059.
762 Kefauver, J.M., Ward, A.B., and Patapoutian, A. (2020). Discoveries in structure and physiology of
763 mechanically activated ion channels. Nature *587*, 567-576.
764 Kudo, M., Melton, A.C., Chen, C., Engler, M.B., Huang, K.E., Ren, X., Wang, Y., Bernstein, X., Li, J.T., Atabai,
765 K.*, et al.* (2012). IL-17A produced by alphabeta T cells drives airway hyper-responsiveness in mice and
766 enhances mouse and human airway smooth muscle contraction. Nat Med *18*, 547-554.
767 La Manno, G., Soldatov, R., Zeisel, A., Braun, E., Hochgerner, H., Petukhov, V., Lidschreiber, K., Kastriti,
768 M.E., Lonnerberg, P., Furlan, A.*, et al.* (2018). RNA velocity of single cells. Nature *560*, 494-498.
769 Langan, E.A., Philpott, M.P., Kloepper, J.E., and Paus, R. (2015). Human hair follicle organ culture: theory,
770 application and perspectives. Exp Dermatol *24*, 903-911.
771 Li, X., Yao, X., Zhu, Y., Zhang, H., Wang, H., Ma, Q., Yan, F., Yang, Y., Zhang, J., Shi, H.*, et al.* (2019). The
772 Caspase Inhibitor Z-VAD-FMK Alleviates Endotoxic Shock via Inducing Macrophages Necroptosis and
773 Promoting MDSCs-Mediated Inhibition of Macrophages Activation. Front Immunol *10*, 1824.
774 Liu, F., Hamer, M.A., Heilmann, S., Herold, C., Moebus, S., Hofman, A., Uitterlinden, A.G., Nothen, M.M.,
775 van Duijn, C.M., Nijsten, T.E.*, et al.* (2016). Prediction of male-pattern baldness from genotypes. Eur J
776 Hum Genet *24*, 895-902.

Liu, X., Chen, W., Zeng, Q., Ma, B., Li, Z., Meng, T., Chen, J., Yu, N., Zhou, Z., and Long, X. (2022). Single-Cell RNA-Sequencing Reveals Lineage-Specific Regulatory Changes of Fibroblasts and Vascular Endothelial Cells in Keloids. J Invest Dermatol *142*, 124-135 e111.

Lolli, F., Pallotti, F., Rossi, A., Fortuna, M.C., Caro, G., Lenzi, A., Sansone, A., and Lombardo, F. (2017). Androgenetic alopecia: a review. Endocrine *57*, 9-17.

Lynch, G.S., and Ryall, J.G. (2008). Role of beta-adrenoceptor signaling in skeletal muscle: implications for muscle wasting and disease. Physiol Rev *88*, 729-767.

Magro, C.M., Rossi, A., Poe, J., Manhas-Bhutani, S., and Sadick, N. (2011). The role of inflammation and immunity in the pathogenesis of androgenetic alopecia. J Drugs Dermatol *10*, 1404-1411.

Martel, J.L., Miao, J.H., and Badri, T. (2023). Anatomy, Hair Follicle. In StatPearls (Treasure Island (FL)).

Martinez-Jacobo, L., Villarreal-Villarreal, C.D., Ortiz-Lopez, R., Ocampo-Candiani, J., and Rojas-Martinez, A. (2018). Genetic and molecular aspects of androgenetic alopecia. Indian J Dermatol Venereol Leprol *84*, 263-268.

Martino, P., Sunkara, R., Heitman, N., Rangl, M., Brown, A., Saxena, N., Grisanti, L., Kohan, D., Yanagisawa, M., and Rendl, M. (2023). Progenitor-derived endothelin controls dermal sheath contraction for hair follicle regression. Nat Cell Biol *25*, 222-234.

Martino, P.A., Heitman, N., and Rendl, M. (2021). The dermal sheath: An emerging component of the hair follicle stem cell niche. Exp Dermatol *30*, 512-521.

Matsumura, H., Mohri, Y., Binh, N.T., Morinaga, H., Fukuda, M., Ito, M., Kurata, S., Hoeijmakers, J., and Nishimura, E.K. (2016). Hair follicle aging is driven by transepidermal elimination of stem cells via COL17A1 proteolysis. Science *351*, aad4395.

Mereu, E., Lafzi, A., Moutinho, C., Ziegenhain, C., McCarthy, D.J., Alvarez-Varela, A., Batlle, E., Sagar, Grun, D., Lau, J.K.*, et al.* (2020). Benchmarking single-cell RNA-sequencing protocols for cell atlas projects. Nat Biotechnol *38*, 747-755.

Morgan, B.A. (2014). The dermal papilla: an instructive niche for epithelial stem and progenitor cells in development and regeneration of the hair follicle. Cold Spring Harb Perspect Med *4*, a015180.

Morinaga, H., Mohri, Y., Grachtchouk, M., Asakawa, K., Matsumura, H., Oshima, M., Takayama, N., Kato, T., Nishimori, Y., Sorimachi, Y.*, et al.* (2021). Obesity accelerates hair thinning by stem cell-centric converging mechanisms. Nature *595*, 266-271.

Nayak, A., Wang, T., Franz, P., Steffen, W., Chizhov, I., Tsiavaliaris, G., and Amrute-Nayak, M. (2020). Single-molecule analysis reveals that regulatory light chains fine-tune skeletal myosin II function. J Biol Chem *295*, 7046-7059.

Ntshingila, S., Khumalo, N.P., Engel, M., and Arowolo, A.T. (2021). An appraisal of laboratory models of androgenetic alopecia: A systematic review. Skin Health Dis *1*, e15.

Oh, J.W., Kloepper, J., Langan, E.A., Kim, Y., Yeo, J., Kim, M.J., Hsi, T.C., Rose, C., Yoon, G.S., Lee, S.J.*, et al.* (2016). A Guide to Studying Human Hair Follicle Cycling In Vivo. J Invest Dermatol *136*, 34-44.

Papalexi, E., and Satija, R. (2018). Single-cell RNA sequencing to explore immune cell heterogeneity. Nat Rev Immunol *18*, 35-45.

Peyravian, N., Deo, S., Daunert, S., and Jimenez, J.J. (2020). The Inflammatory Aspect of Male and Female Pattern Hair Loss. J Inflamm Res *13*, 879-881.

Plikus, M.V. (2012). New activators and inhibitors in the hair cycle clock: targeting stem cells' state of competence. J Invest Dermatol *132*, 1321-1324.

Plikus, M.V., and Chuong, C.M. (2014). Macroenvironmental regulation of hair cycling and collective regenerative behavior. Cold Spring Harb Perspect Med *4*, a015198.

821 Potter, S.S. (2018). Single-cell RNA sequencing for the study of development, physiology and disease.
822 Nat Rev Nephrol *14*, 479-492.
823 Qiu, X., Mao, Q., Tang, Y., Wang, L., Chawla, R., Pliner, H.A., and Trapnell, C. (2017). Reversed graph
824 embedding resolves complex single-cell trajectories. Nat Methods *14*, 979-982.
825 Rahmani, W., Abbasi, S., Hagner, A., Raharjo, E., Kumar, R., Hotta, A., Magness, S., Metzger, D., and
826 Biernaskie, J. (2014). Hair follicle dermal stem cells regenerate the dermal sheath, repopulate the
827 dermal papilla, and modulate hair type. Dev Cell *31*, 543-558.
828 Ranade, S.S., Syeda, R., and Patapoutian, A. (2015). Mechanically Activated Ion Channels. Neuron *87*,
829 1162-1179.
830 Takahashi, R., Grzenda, A., Allison, T.F., Rawnsley, J., Balin, S.J., Sabri, S., Plath, K., and Lowry, W.E. (2020).
831 Defining Transcriptional Signatures of Human Hair Follicle Cell States. J Invest Dermatol *140*, 764-773
832 e764.
833 Wu, S., Yu, Y., Liu, C., Zhang, X., Zhu, P., Peng, Y., Yan, X., Li, Y., Hua, P., Li, Q.*, et al.* (2022). Single-cell
834 transcriptomics reveals lineage trajectory of human scalp hair follicle and informs mechanisms of hair
835 graying. Cell Discov *8*, 49.
836 Xie, Y., Chen, D., Jiang, K., Song, L., Qian, N., Du, Y., Yang, Y., Wang, F., and Chen, T. (2022). Hair shaft
837 miniaturization causes stem cell depletion through mechanosensory signals mediated by a Piezo1-
838 calcium-TNF-alpha axis. Cell Stem Cell *29*, 70-85 e76.
839 Yang, H., Adam, R.C., Ge, Y., Hua, Z.L., and Fuchs, E. (2017). Epithelial-Mesenchymal Micro-niches
840 Govern Stem Cell Lineage Choices. Cell *169*, 483-496 e413.
841 Zou, Z., Long, X., Zhao, Q., Zheng, Y., Song, M., Ma, S., Jing, Y., Wang, S., He, Y., Esteban, C.R.*, et al.* (2021).
842 A Single-Cell Transcriptomic Atlas of Human Skin Aging. Dev Cell *56*, 383-397 e388.
843
844
845
846
847
848
849
850
851
852
853
854
855
856
857

858 **Figures and Figure legends**

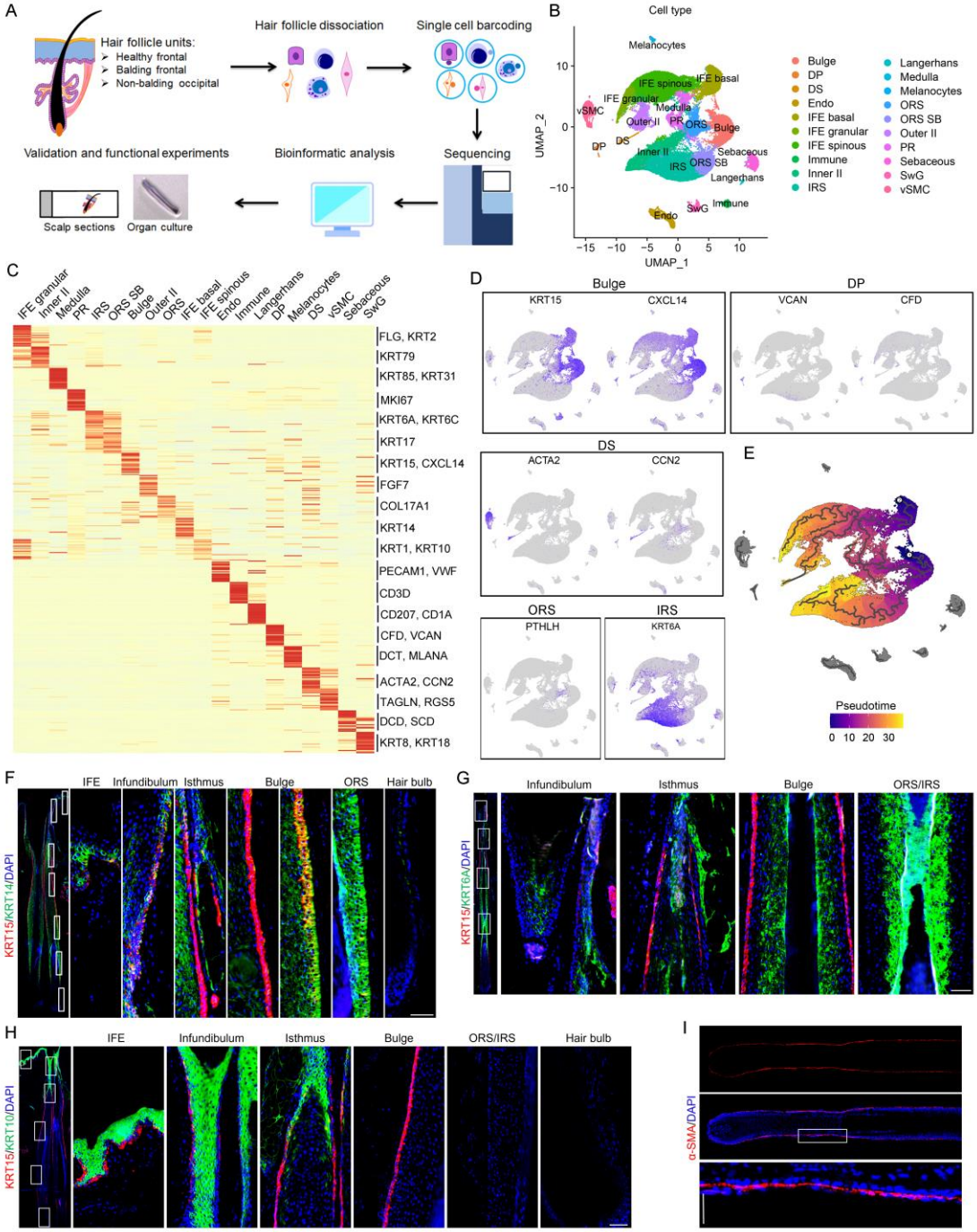

859

860 **Fig. 1: scRNA-seq reveals cell type composition in anagen HF units of**
861 **AGA and healthy scalps.**

862 **A** Flowchart overview of scRNA-seq, and subsequent validation and functional
863 experiments with anagen HFs from balding frontal and non-balding occipital
864 scalps of AGA patients, and normal scalps of healthy individuals. **B** Uniform
865 manifold approximation and projection (UMAP) plot showing the twenty cell

866 types of human anagen HFs. DP, dermal papilla; DS, dermal sheath; Endo,
867 endothelial cells; IFE, interfollicular epidermis; Inner II, inner layer of
868 infundibulum and isthmus; IRS, inner root sheath; ORS, outer root sheath basal;
869 ORS SB, outer root sheath suprabasal; Outer II, outer layer of infundibulum and
870 isthmus; PR, proliferating progenitors; SwG, sweat gland; vSMC, vascular
871 smooth muscle cells. **C** Heatmap of top 20 marker genes of each HF cell type.
872 **D** Feature plots showing expression of marker genes for the Bulge (KRT15,
873 KRT14), DP (VCAN, CFD), DS (ACTA2, CCN2), ORS (PTHLH), IRS (KRT6A).
874 **E** Monocle3 pseudotime of all HF cell types. **F-I** Representative immunostaining
875 images of KRT15/KRT14 (**F**), KRT6A/KRT15 (**G**), KRT15/KRT10 (**H**) and α-
876 SMA (**I**) in human HF sections and the corresponding magnified views of boxed
877 areas. (n=5 HFs from 3 individuals. The same 3 individuals' samples were used
878 in all following HF stainings unless otherwise noted). Scale bar: 50 μm.

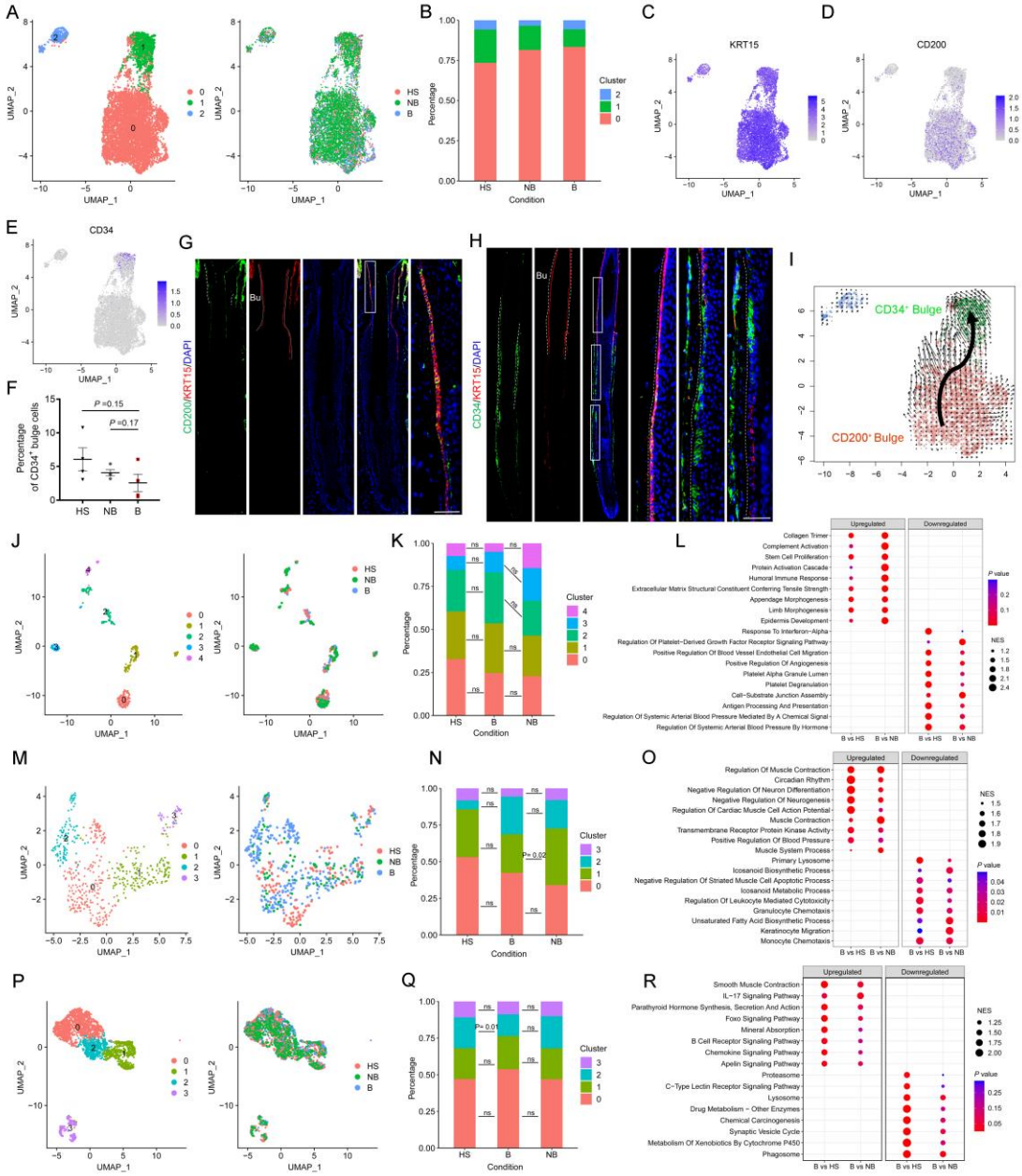

Fig. 2: Heterogeneity of cell subpopulations in AGA and healthy scalps. **A** UMAP plots showing subclusters and sample conditions of bulge cells. **B** Bar graph representing the percentage of subpopulations of bulge cells. **C-E** Feature plots showing the expression of the KRT15 (**C**), CD200 (**D**) and CD34 (**E**) in bulge cells. **F** The ratio of CD34⁺ bulge cells in Healthy (HS), non-balding (NB) and balding (B) conditions. **G, H** Representative images showing CD200 protein expression in upper bulge stem cells (**G**) and CD34 in progenitor cells (**H**). Right panels, magnified images of boxed areas. Bu, bulge. Red, KRT15 (K15) staining. DAPI staining (blue) indicates nuclear localization. ORS–DS

889 boundary is indicated by dashed lines. Scale bar: 50 μm. **I** velocyto showing
890 the single-cell trajectories of bulge subclusters in UMAP. **J** UMAP plots showing
891 subclusters and sample conditions of DP cells. **K** Bar graph representing the
892 percentage of subpopulations of DP cells. **L** Representative GO terms of
893 upregulated (left) and downregulated (right) DEGs between balding and healthy
894 groups (B vs HS), balding and non-balding groups (B vs NB) in DP cells. NES
895 stands for enrichment scores. The color keys from red to blue indicate the range
896 of P value. **M** UMAP plot showing subclusters and sample conditions of DS
897 cells. **N** Bar graph representing the percentage of subpopulations of DS cells.
898 **O** Representative GO terms enriched in balding versus non-balding or healthy
899 DS cells. NES stands for enrichment scores. The color keys from red to blue
900 indicate the range of p value. e. **P** UMAP plot showing subclusters and sample
901 conditions of vSMC cells. **Q** Bar graph representing the percentage of
902 subpopulations of vSMC cells. **R** Representative GO terms enriched in balding
903 versus non-balding or healthy vSMC cells. NES stands for enrichment scores.
904 The color keys from red to blue indicate the range of p value. The data represent
905 the means±SEM. P values were determined by unpaired (B vs HS) or paired (B
906 vs NB) student's t-test. ns, not significant.

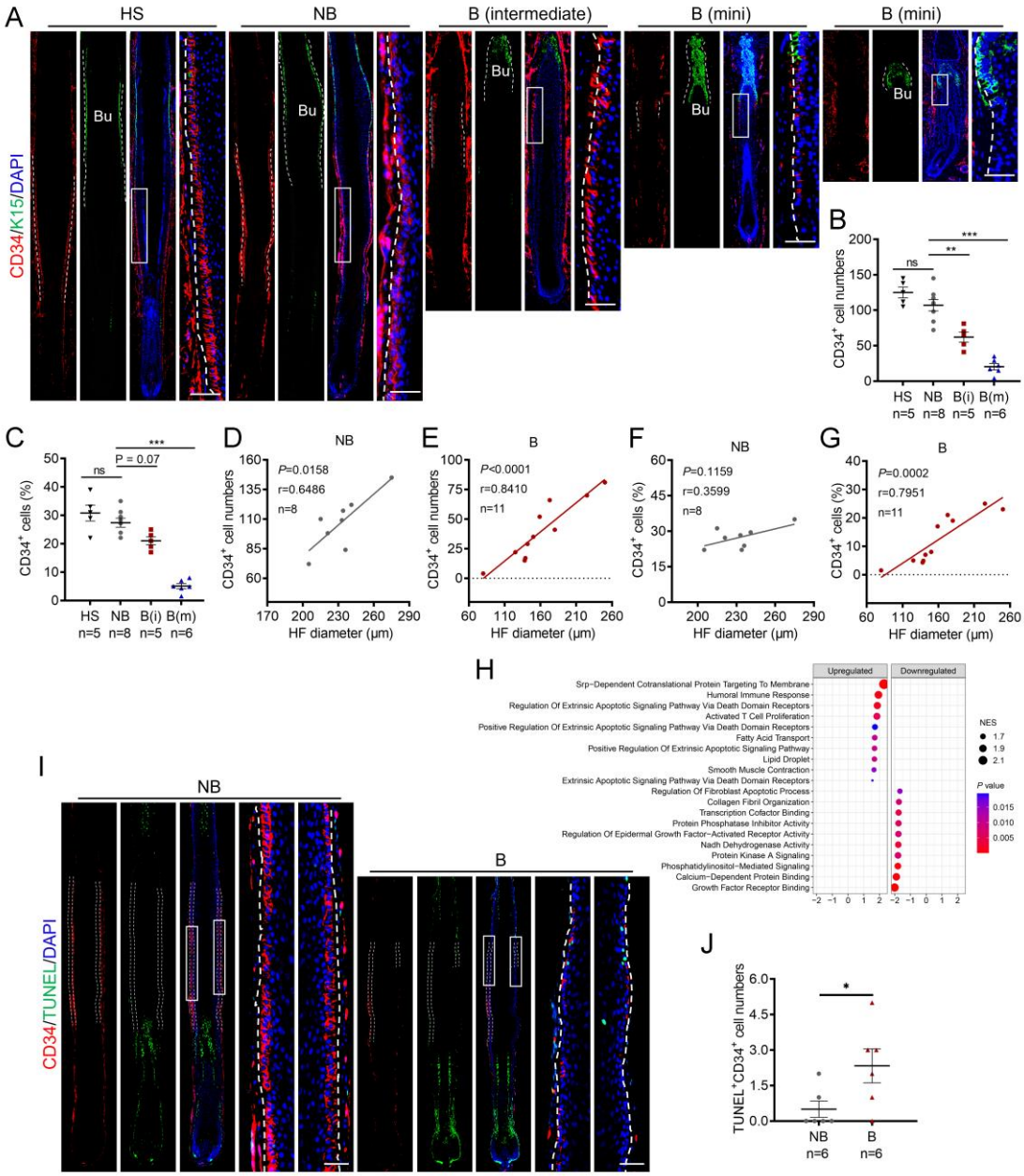

Fig. 3: Apoptotic loss of HF progenitor cells is associated with HF miniaturization in AGA.

A Immunostaining images show progenitor cells in terminal HFs of occipital scalps from healthy individuals (n=5 anagen HFs from 3 individuals), terminal HFs of non-balding occipital scalps (n=8 anagen HFs) and intermediate/mini HFs of balding frontal scalps (n=11 anagen HFs) from 3 AGA patients. Bulge HFSCs and progenitor cells were labelled with K15 (green) and CD34 (red) respectively and indicated by the dotted line. Right panels, magnified images of boxed areas. Bu, bulge. Types of HFs were defined by their diameter.

917 Terminal: diameter>200 μm; Intermediate: 150 μm <diameter<200 μm; mini:
918 diameter<150 μm. **B, C** Quantification of the number (**B**) of $CD34^+$ progenitor
919 cells in different groups and their proportion in the total outer layer of HFs (**C**).
920 **D-G** Scatter plots show the correlation between HF diameters and the number
921 or percentage of $CD34^+$ progenitor cells in AGA patients. Spearman's
922 correlation coefficient was used for the correlation analysis (two-tailed). **H**
923 Top10 GO terms upregulated or downregulated in B versus in NB $CD34^+$
924 progenitor cells. NES stands for enrichment scores. The color keys from red to
925 blue indicate the range of P value. **I, J** Representative images of TUNEL
926 staining on anagen HFs from non-balding occipital scalps and balding frontal
927 scalps of AGA patients (n=6 HFs from 3 donors for each group); Right panels,
928 magnified images of boxed areas (**I**). The quantification of $TUNEL^+CD34^+$ cell
929 numbers in two groups (**J**). Progenitor cells were indicated with dotted line.
930 Scale bar: 50μm. The data represent the means±SEM. *p<0.05, **p<0.01,
931 ***p<0.001, determined by one-way ANOVA with Tukey's post hoc test (**B, C**)
932 or unpaired Student's t-test (**J**). ns, not significant.

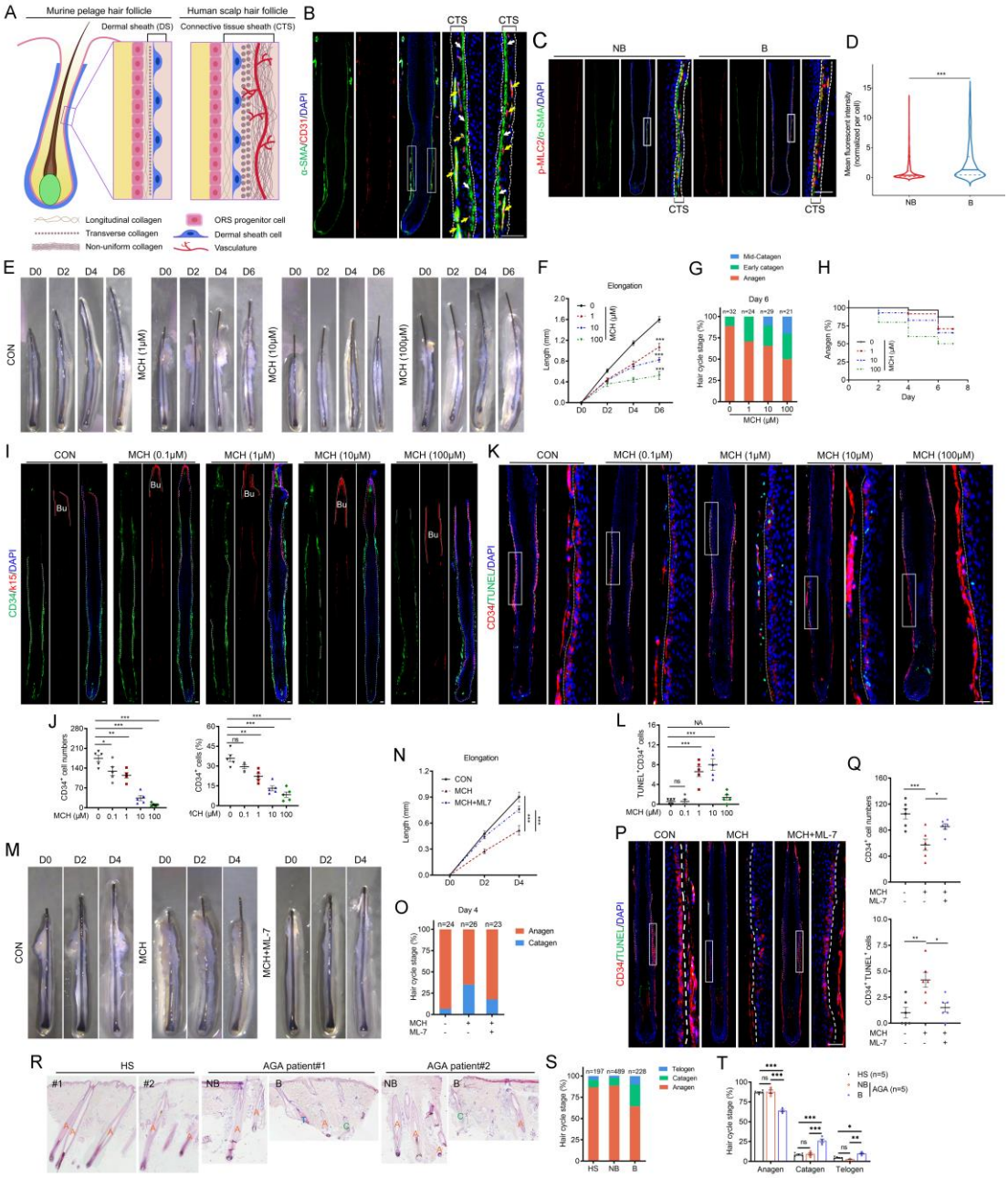

Fig. 4: Hyperactive CTS contraction induces premature hair regression in AGA.

A Dermal sheath (DS)/ connective tissue sheath (CTS) in murine pelage follicle/ human scalp follicle. In murine pelage follicle (left), the DS is the outer layer of the ORS progenitors. In human scalp follicle, the outer layer is the CTS (right), which is mainly composed of DS cells, vasculature and multiple types of collagens. **B** Immunostaining of CD31 (an endothelial cell marker) and α-SMA (a marker for both DS and vSMC cells) in human anagen HFs. CTS is located

942 between the two dotted lines. White arrows indicate DS. Yellow arrows indicate
943 blood vessels. Right panels, magnified images of boxed areas. **C** The activation
944 of DS muscle contraction was evaluated with p-MLC2 immunostaining on
945 anagen HFs from non-balding occipital scalps (n=5 HFs) and balding frontal
946 scalps (n=6 HFs) of 3 AGA patients. Right panels, magnified images of boxed
947 areas. **D** Quantification of relative mean fluorescent intensity (RFI) of p-MLC2
948 in α-SMA positive cells in CTS in different groups. **E** Representative images of
949 hair shaft elongation of human HFs ex vivo with vehicle (CON) or MCH
950 treatment at concentration of 0.1 μM, 1 μM, 10 μM, 100 μM as indicated (n=21-
951 32 HFs from 3 donors for each group). The same individuals' HF samples were
952 used in the following staining of HFs with the same treatments. **F** Quantification
953 of hair shaft elongation on day 2/4/6 with indicated treatments (n=32/24/29/21
954 in different groups respectively). **G** Macroscopic quantification of hair cycle
955 stage of HFs with vehicle or MCH treatments on day 6. **H** Percentages of HFs
956 in anagen on day 2/4/6 with indicated treatments. **I** Representative images of
957 co-immunostaining of CD34 (green) and K15 (red) in HFs with vehicle or MCH
958 treatments. Progenitor cells and bulge cells were indicated by dotted lines on
959 green and red single-channel IF images, respectively. **J** Quantification of $CD34^+$
960 progenitor cells numbers and proportions in the total outer layer of HFs with
961 vehicle or MCH treatments. **K** Apoptosis of progenitor cells with vehicle or MCH
962 treatment were indicated with co-immunostaining of CD34 and TUNEL.
963 Progenitor cells were indicated with dotted line. Right panels, magnified images
964 of boxed areas. **L** Quantification of $TUNEL^+CD34^+$ progenitor cells in HFs
965 treated with vehicle or MCH. To be mentioned, $TUNEL^+CD34^+$ progenitor cells
966 are barely detectable under 100 μM MCH administration because CD34+
967 progenitor cells were almost vanished under this condition. **M** Representative
968 images of hair shaft elongation of human HFs ex vivo with vehicle or MCH (10
969 μM) and ML-7 (0.3 μM) treatment as indicated (n=23-26 HFs from 3 donors for
970 each group, independent experiments). **N** Quantification of hair shaft elongation
971 on day 2/4 with vehicle or MCH and ML-7 treatments (n=24/26/23 in different

groups respectively). **O** Macroscopic quantification of hair cycle stage of HFs with vehicle or MCH and ML-7 treatments on day 4. **P** Co-immunostaining of CD34 and TUNEL showed progenitor cell apoptosis with indicated treatments (n=6 HFs from 3 donors for each group). Right panels, magnified images of boxed areas. **Q** Quantification of total and apoptotic $CD34^+$ progenitor cells numbers in HFs with vehicle or MCH and ML-7 treatments. **R** Representative images of HE staining with HS frontal scalps, NB occipital and B frontal scalps from AGA patients. A, anagen HF. C, catagen HF. T, telogen HF. **S** Macroscopic quantification of hair cycle stage of HFs in HE staining (n=197/489/228 HFs from 5 HS and 5 AGA donors). **T** Percentage of anagen, catagen and telogen HFs in HS, NB and B scalps (n=197/489/228 HFs from 5 HS and 5 AGA donors). Scale bar, 50 μm. Data are expressed as mean±SEM and were analyzed by one-way ANOVA with Tukey's post hoc test (J, L, Q, T) and two-way ANOVA with a post hoc Holm–Sidak's multiple comparisons test (F, N), or unpaired Student's t-test (D). *$p<0.05$, **$p<0.01$, ***$p<0.001$. ns, not significant. NA, not applicable.

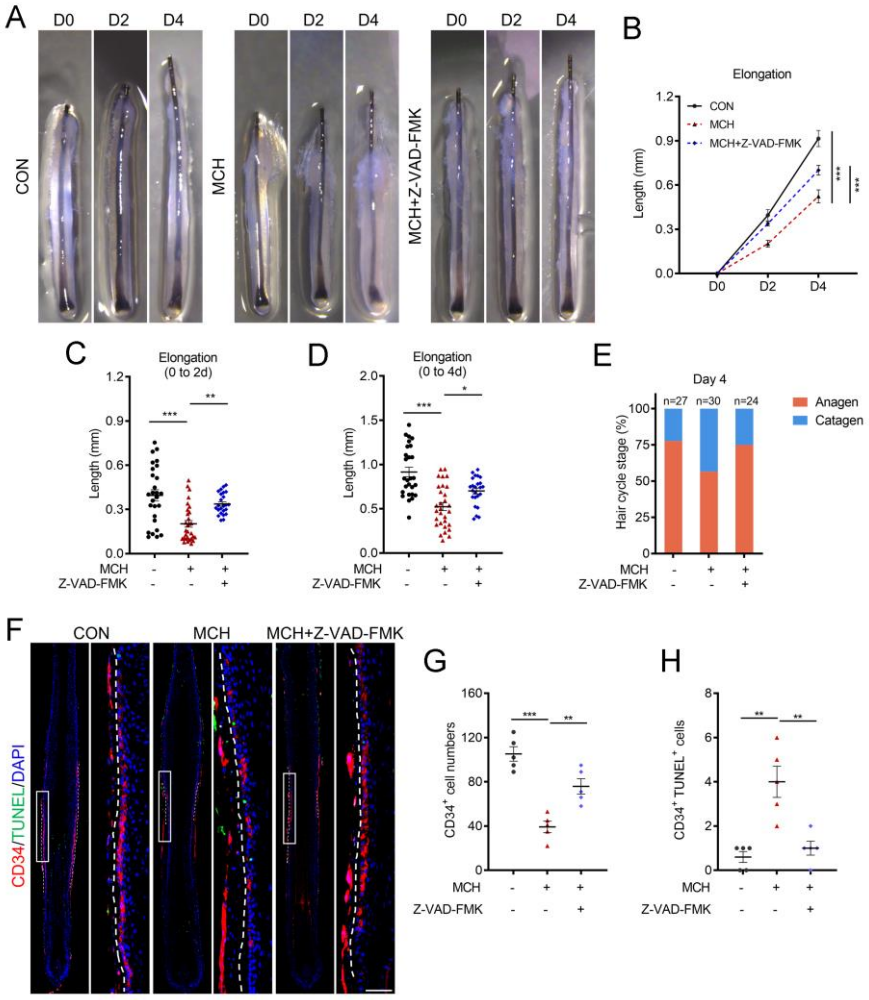

Fig. 5: CTS contraction drives premature hair regression in an apoptosis-dependent manner.

A Representative images of hair shaft elongation of human HFs ex vivo with or without MCH (10 μM) and Z-VAD-FMK (10 μM) as indicated (n=24-30 anagen HFs from 3 donors for each group). The same individuals' HF samples were used in the following staining of HFs with the same treatments. **B** Quantification of hair shaft elongation on day 2/4/6 with indicated treatments. **C, D** Scatter plots show the elongation length of hair shaft with indicated treatments on day 2 (**C**) and day 4 (**D**). **E** Macroscopic quantification of hair cycle stage of HFs with indicated treatments on day 4. **F** Co-immunostaining of CD34 and TUNEL showed apoptosis of progenitor cells with indicated treatments (n=5 HFs for each group from 3 individuals). Progenitor cells were indicated with dotted line. Right panels, magnified images of boxed areas. **G, H** Quantification of total (G)

and apoptosis (H) CD34⁺ progenitor cell numbers in HFs with indicated treatments. Scale bar: 50 μm. The data represent the means±SEM. *p<0.05, **p<0.01, ***p<0.001, determined by one-way ANOVA with Tukey's post hoc test (C, D, G, H) and two-way ANOVA with a post hoc Holm–Sidak's multiple comparisons test (B).

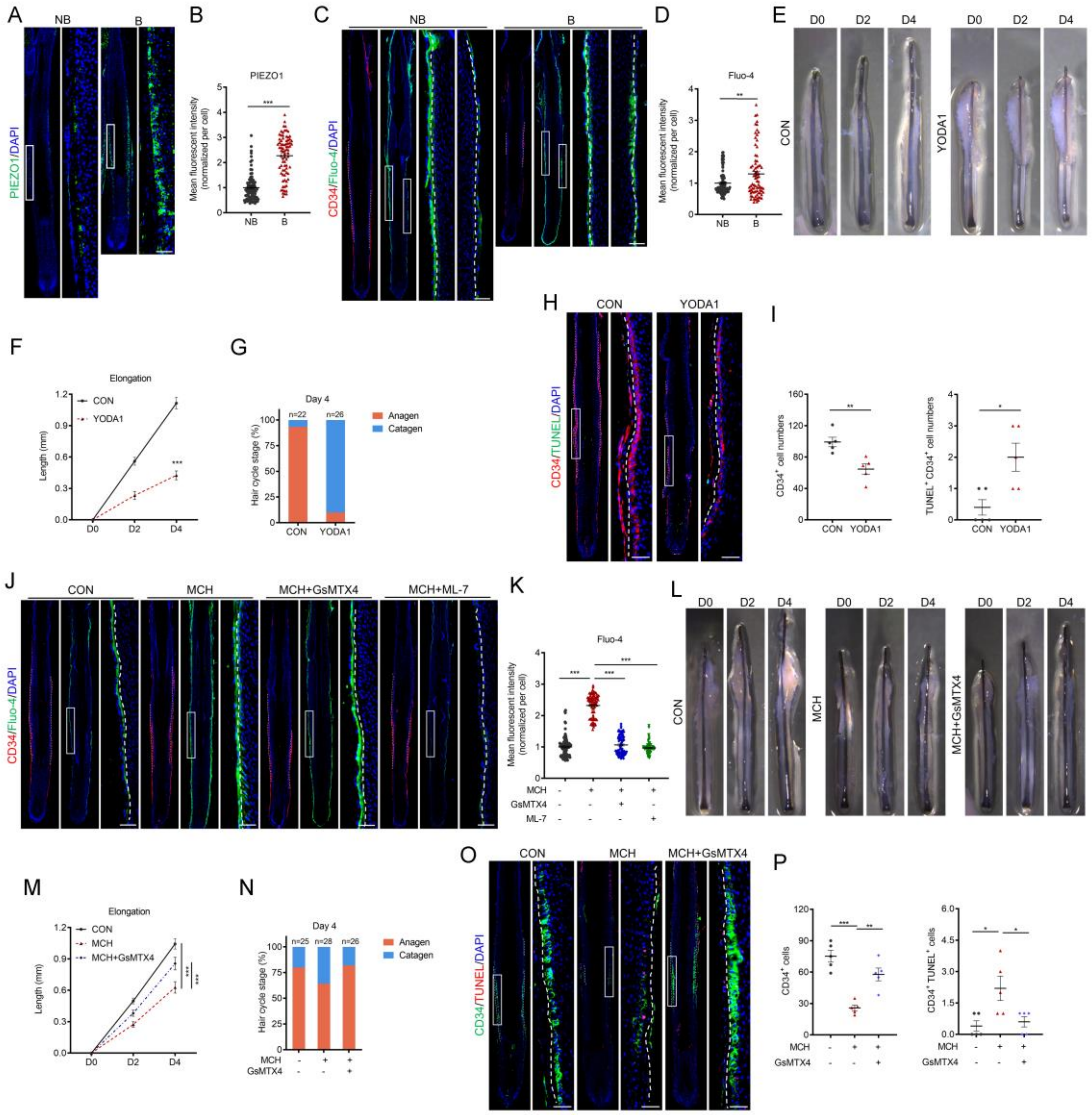

Fig. 6: PIEZO1 signaling is necessary for CTS contraction-induced progenitor cell apoptosis and premature hair regression.

A, B (**A**) Representative immunostaining of PIEZO1 on skin sections from balding frontal and non-balding occipital scalps of AGA patients (n=3) and (**B**) the quantification of mean fluorescent intensity in outermost layer of mid-HF

1014 cells (n=70-90 cells from 3 patients). **C, D** (**C**) CD34 and Fluo-4 staining were
1015 performed on serial sections from balding frontal and non-balding occipital
1016 scalps of AGA patients (n=3) and (**D**) the Fluo-4 mean fluorescent intensity in
1017 $CD34^+$ progenitor cells was quantified (n=100 cells in non-balding HFs and 80
1018 cells in balding HFs from 3 patients). Fluo-4 indicates the cellular Ca^{2+}
1019 concentration. **E** Representative images of hair shaft elongation of human HFs
1020 ex vivo with or without YODA1 (15 μM) as indicated (n=22-26 anagen HFs from
1021 3 individuals for each group). The same individuals' HF samples were used in
1022 the following staining of HFs with the same treatments. **F** Quantification of hair
1023 shaft elongation on day 2/4 with vehicle or YODA1 treatments. **G** Macroscopic
1024 quantification of hair cycle stage of HFs with YODA1 treatment on day 4. **H** Co-
1025 immunostaining of CD34 and TUNEL showed apoptosis of progenitor cells with
1026 YODA1 treatment. 5 HFs from 3 individuals were performed with
1027 immunostaining. **I** Quantification of total and apoptotic $CD34^+$ progenitor cell
1028 numbers in HFs treated with YODA1. **J, K** (**J**) CD34 and Fluo-4 staining were
1029 performed on serial sections of HFs with indicated treatments (n=3 HFs for each
1030 group) and (**K**) the Fluo-4 mean fluorescent intensity in $CD34^+$ progenitor cells
1031 was quantified (n=80-100 cells from 3 different HFs). **L** Representative
1032 images of hair shaft elongation of human anagen HFs ex vivo treated with MCH
1033 (10 μM) and GsMTX4(1 μM) (n=25 HFs for CON, 28 HFs for MCH and 26 HFs
1034 for MCH+GsMTX4; from 3 individuals). The same individuals' HF samples were
1035 used in the following staining of HFs with the same treatments. **M** Quantification
1036 of hair shaft elongation on day 2/4 with MCH and GsMTX4 treatments. **N**
1037 Macroscopic quantification of hair cycle stage of HFs with MCH and GsMTX4
1038 treatments on day 4. **O** Co-immunostaining of CD34 and TUNEL showed
1039 apoptosis of progenitor cells with MCH and GsMTX4 treatments. 5 HFs from 3
1040 individuals were performed with staining. **P** Quantification of total and apoptotic
1041 $CD34^+$ progenitor cell numbers in HFs treated with MCH and GsMTX4. Right
1042 panels, magnified images of boxed areas. Scale bar: 50 μm. Data are
1043 expressed as mean±SEM and were analyzed by one-way ANOVA with Tukey's

post hoc test (K, P), two-way ANOVA with a post hoc Holm–Sidak's multiple comparisons test (F, M), and two-tailed unpaired Student's t-test (B, D, I). *p<0.05, **p<0.01, ***p<0.001.

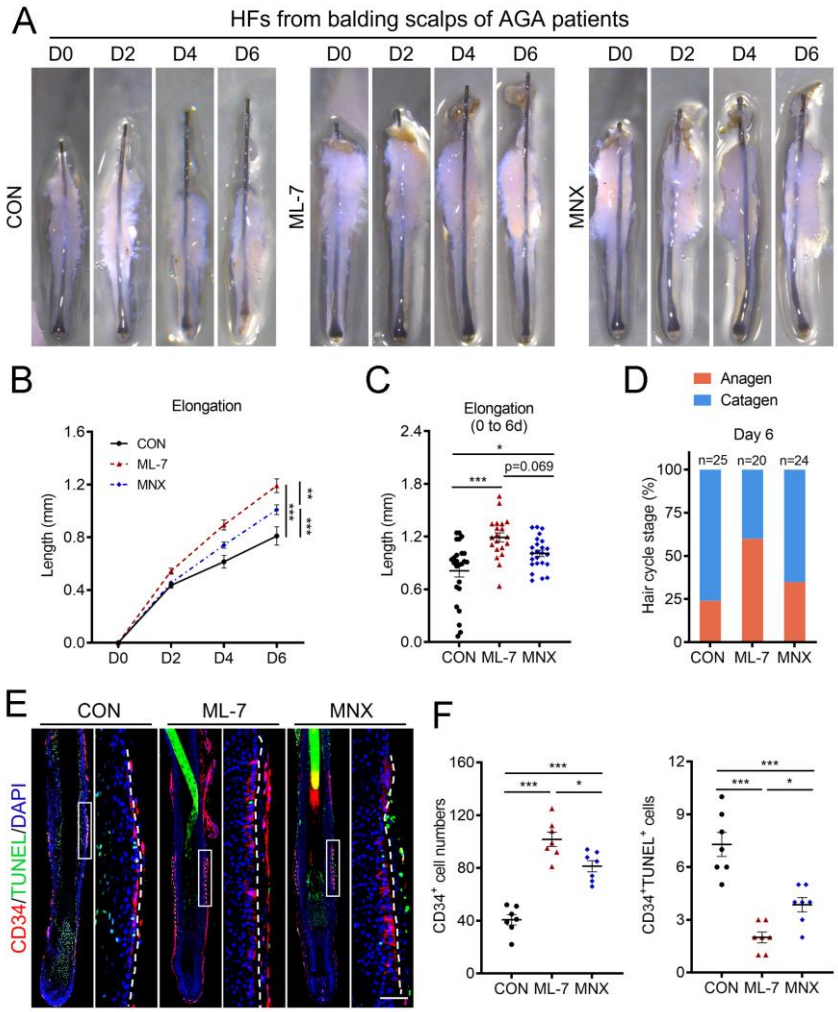

Fig. 7: ML-7 exhibits a better effect than MNX on promoting the growth of HFs from the balding scalps of AGA patients.

A Representative images of hair shaft elongation of anagen HFs from balding scalps of AGA patients ex vivo treated with vehicle (CON), ML-7 (0.3 μM) or minoxidil (MNX) ((100 μM)) as indicated (n=31-37 balding HFs from 5 AGA patients for each group). 3 patients' HF samples were used in the following staining. **B** Quantification of hair shaft elongation on day 2/4/6 with indicated treatments. **C** Scatter plots show the elongation length of hair shaft on day 6. **D** Macroscopic quantification of hair cycle stage of HFs with indicated treatments

1058 on day 6. **E** Co-immunostaining of CD34 and TUNEL showed apoptosis of
1059 progenitor cells with indicated treatments (n=7 balding HFs from 3 AGA patients
1060 for each group). Right panels, magnified images of boxed areas. **F**
1061 Quantification of total and apoptosis $CD34^+$ progenitor cell numbers in HFs with
1062 indicated treatments. Scale bar: 50 μm. The data represent the means±SEM.
1063 *p<0.05, **p<0.01, ***p<0.001, determined by one-way ANOVA with Tukey's
1064 post hoc test (C, F) and two-way ANOVA with a post hoc Holm–Sidak's multiple
1065 comparisons test (B).
1066
1067